NOLTA, IEICE

Invited Review Paper

Nonlinear dynamics of ship capsizing at sea

Atsuo Maki [1 a)], *Yuu Miino* [2], *Naoya Umeda* [1], *Masahiro Sakai* [1], *Tetsushi Ueta* [3], *and Hiroshi Kawakami* [4]

[1] *Department of Naval Architecture and Ocean Engineering, Graduate School of Engineering, Osaka University, 2-1 Yamadaoka, Suita, Osaka 565-0971, Japan*

[2] *Department of Electric and Electronic Engineering, School of Engineering, Tokyo University of Technology, 1404-1 Katakuramachi, Hachioji, Tokyo 192-0914, Japan*

[3] *Center for Administration of Information Technology, Tokushima University, 2-1 Minami-Josanjima-Cho, Tokushima 770-8506, Japan*

[4] *Professor Emeritus of Tokushima University*

[a)] *maki@naoe.eng.osaka-u.ac.jp*

Received April 10, 2021; Revised July 25, 2021; Published January 1, 2022

Abstract: Capsizing is one of the worst scenarios in oceangoing vessels. It could lead to a high number of fatalities. A considerable number of studies have been conducted until the 1980s, and one of the discoveries is the weather criterion established by the International Maritime Organization (IMO). In the past, one of the biggest difficulties in revealing the behavior of ship-roll motion was the nonlinearity of the governing equation. On the other hand, after the mid-1980s, the complexity of the capsizing problem was uncovered with the aid of computers. In this study, we present the theoretical backgrounds of the capsizing problem from the viewpoint of nonlinear dynamics. Then, we discuss the theoretical conditions and mechanisms of the bifurcations of periodic solutions and numerical attempts for the bifurcations and capsizing.

Key Words: capsizing, regular sea, safe-basin boundary, global bifurcation

1. Introduction

Capsizing is one of the most dangerous phenomena for vessels on seas. It could lead to severe fatalities. For instance, when the cruise ferry "*M.V. ESTONIA*" capsized in the Baltic Sea in 1994, the total fatalities was 852 [1]. Therefore, it is essential to prevent the capsizing of oceangoing vessels to ensure safe transportation.

The International Maritime Organization (IMO), a specialized United Nations agency, is responsible for the criteria that improve the safety of vessels. The Weather Criterion of Assembly Resolution A.562 of IMO is almost the same as the domestic criterion in Japan. In this criterion, energy balance between external and restoring moments is employed, and direct manipulation of the nonlinear differential

Nonlinear Theory and Its Applications, IEICE, vol. 13, no. 1, pp. 2–24 DOI: 10.1587/nolta.13.2

equation of ship-roll motion in beam seas is avoided by introducing the potential energy of restoring moments. Therefore, the nonlinearity of the system is well organized in the criteria.

On the other hand, to analyze the capsizing phenomenon further, the knowledge of nonlinear dynamics is essential. Nonlinear oscillators, such as the Duffing equation, are commonly analyzed in other engineering disciplines, such as electrical engineering [2]. The best characteristic of a nonlinear oscillator in naval architecture is the softening behavior in its restoring term. For instance, the softening behavior commonly appears in a pendulum motion. However, for nonlinear oscillators in naval architecture, escaping from a potential well appears as capsizing, which in actual vessels, leads to catastrophic results.

Since the mid-1980s, it has been well-known that capsizing can be triggered by chaotic motions. In naval architecture, one of the pioneering studies on nonlinear dynamical system theory was reported by Nayfeh and Khdeir [3, 4]. They employed a second-order perturbation technique and Floquet theory to predict the period-doubling bifurcation that could lead to chaotic oscillations. Nayfeh and Sanchez revealed the existence of strong initial dependency of the roll response in a regular beam sea on the following seas, and basin boundary metamorphoses were reported [5]. Thompson studied the escape (the same as capsizing) from potential wells for a simple cubic potential and reported fractal metamorphoses and chaotic motions prior to escape [6, 7]. Further, Thompson [7] employed Melnikov's method [8, 9] to analytically estimate the homoclinic tangency. Virgin also pointed out the existence of chaotic behavior in the roll motion in regular seas [10–12]. Further, Virgin conducted a detailed stability analysis for the periodic solution and derived useful criteria [11].

In the 1990s, research on this area accelerated further. Kan and Taguchi reported the capsizing after period-doubling bifurcation in model experiments [13], and theoretical and numerical analyses were conducted [14]. Francescutto also reported the jump phenomenon of the periodic solution in a towing tank experiment [15]. Falzarano conducted the Melnikov analysis on homoclinic and heteroclinic orbits [16]. Bikdash et al. also conducted Melnikov's analysis on the general roll-damping cases [17]. Hsieh et al. extended the Melnikov's method to random excitation. Then, combining the Melnikov analysis and phase space flux, the probability of capsizing was calculated [18]. Murashige and Aihara conducted experiments on a flooded ship. Then, from the measured time-histories, the Lyapunov exponents were calculated, and they revealed the existence of a chaotic attractor [19]. Further, through detailed numerical simulations, the existence of a strange attractor was revealed [20]. Since 2000, further contributions have been reported by Wu and McCue [21]. Maki et al. [22–24], etc.

Herein, we present the theoretical background of the capsizing problem from the viewpoint of nonlinear dynamics.

2. Ship stability

Figure 1 shows a two-dimensional section of a vessel floating on calm water. Herein, it is assumed that the ship is wall-sided and symmetrical along the transverse direction and the angle of the roll is ϕ. For these assumptions, two water lines before and after the inclination intersect at O on the centerline. Here, $\triangle$POQ is the exposed part, whereas $\triangle$P$'$OQ$'$ is the immersed part. When a ship is heeled, the area of $\triangle$POQ is shifted to the area of $\triangle$P$'$OQ$'$. g and g$'$ are the centers of both areas, and notice that, $\triangle$POQ and $\triangle$P$'$OQ$'$ are identical. Owing to shift in the area from $\triangle$POQ to $\triangle$P$'$OQ$'$, the center of buoyancy also shifts from B_0 to B_1. The down arrow from G indicates the gravity force, and that pointing up from B_1 indicates the buoyancy force. Note that the lengths of the two vectors are the same since the weight does not change before and after the inclination, and the ship mass is defined as $W\,[\,\mathrm{kg}\,]$. Here, let us consider the restoring moment around the center of gravity of the vessel G. Its moment is calculated by $W \cdot GZ$. As can be understood, GZ is an important parameter representing the restoring moment, and it is called *Righting arm* or *Righting lever*.

Figure 2 shows the change in GZ curve associated with change in roll angle. As can be seen, with increase in roll angle, GZ decrease and finally becomes zero or negative. It clearly means the softening characteristic of GZ curve, that is the restoring curve.

The importance of GZ in three-dimensional vessels is the same as above. In Fig. 3, the angle

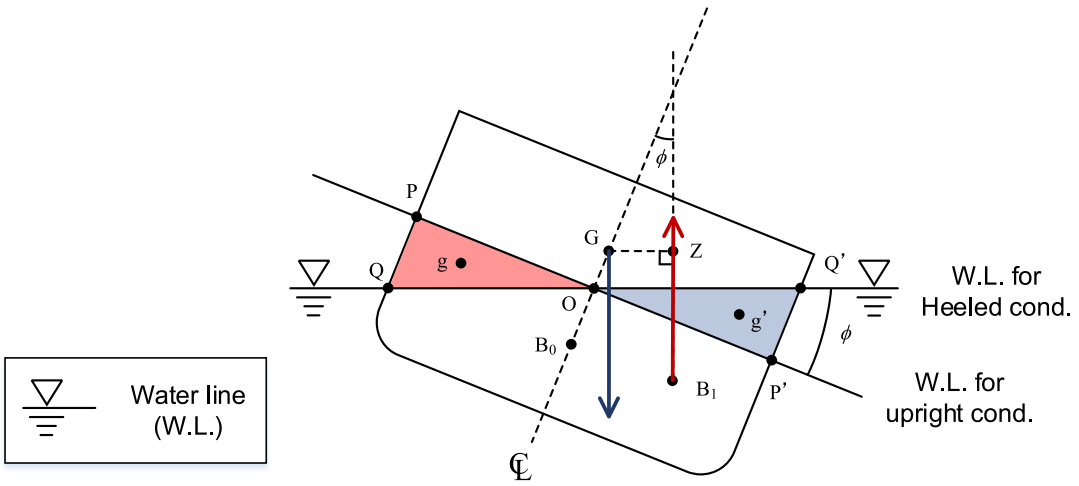

Fig. 1. Restoring moment for a wall-sided vessel.

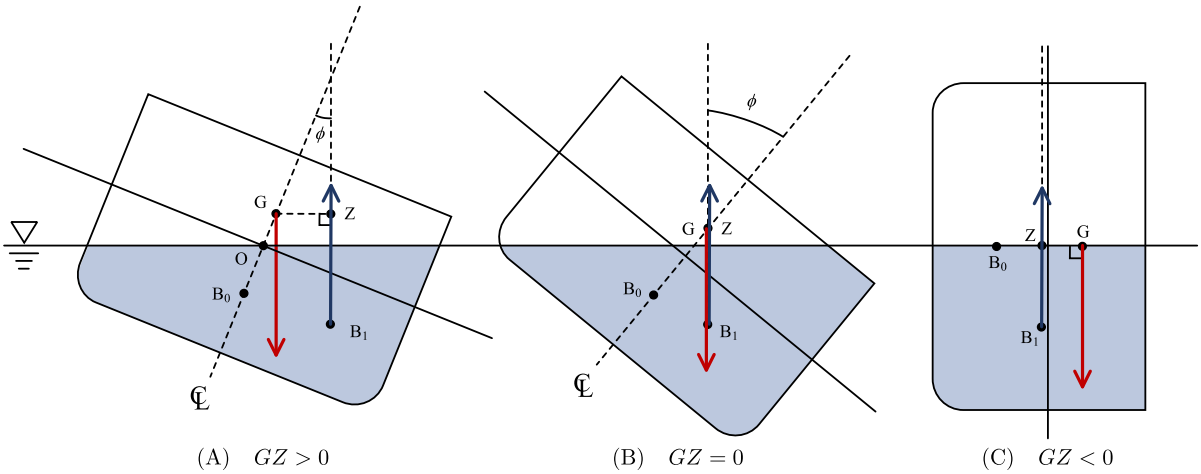

Fig. 2. Change in GZ.

of the roll is ϕ. Typical $GZ\,[\mathrm{m}]$ form is also shown in the lower right panel. As explained above, $W \cdot GZ\,[\mathrm{kg \cdot m}]$ is the restoring moment. Here, $W\,[\mathrm{kg}]$ is the ship mass. As shown in the figure, GZ has three crossing points. $0\,[\mathrm{deg}]$ and $180\,[\mathrm{deg}]$ are stable equilibrium points, whereas ϕ_V, the vanishing stability angle, is an unstable equilibrium point. For theoretical considerations, GZ curve is sometimes approximated by polynomials:

$$GZ\,(\phi) = \sum_{i=0}^{n} c_i \phi^i \tag{1}$$

Practically, n of 3∼5 is chosen.

Next, the external moment is explained. The time-varying external moment acting on the ship hull is derived from waves and winds. In this study, the time-varying wind moment is ignored for brevity, and we assume the regular wave condition. The deformation of the water surface around a vessel changes periodically in the restoring moment. The restoring moment could be evaluated with the relative roll angle to the effective wave slope angle. Since waves are regular and sinusoidal, the external wave moment is a sinusoidal function such as

$$M_{\mathrm{wave}}(t) = M \cos \omega t \tag{2}$$

As shown in Fig. 3 and Eq. (1), the form of the GZ curve is highly nonlinear. For this general form of the GZ curve, the analytical solution cannot be easily found. To overcome this challenge, the intact stability code was constructed based on the energy balance method. We briefly explain the framework of the stability code.

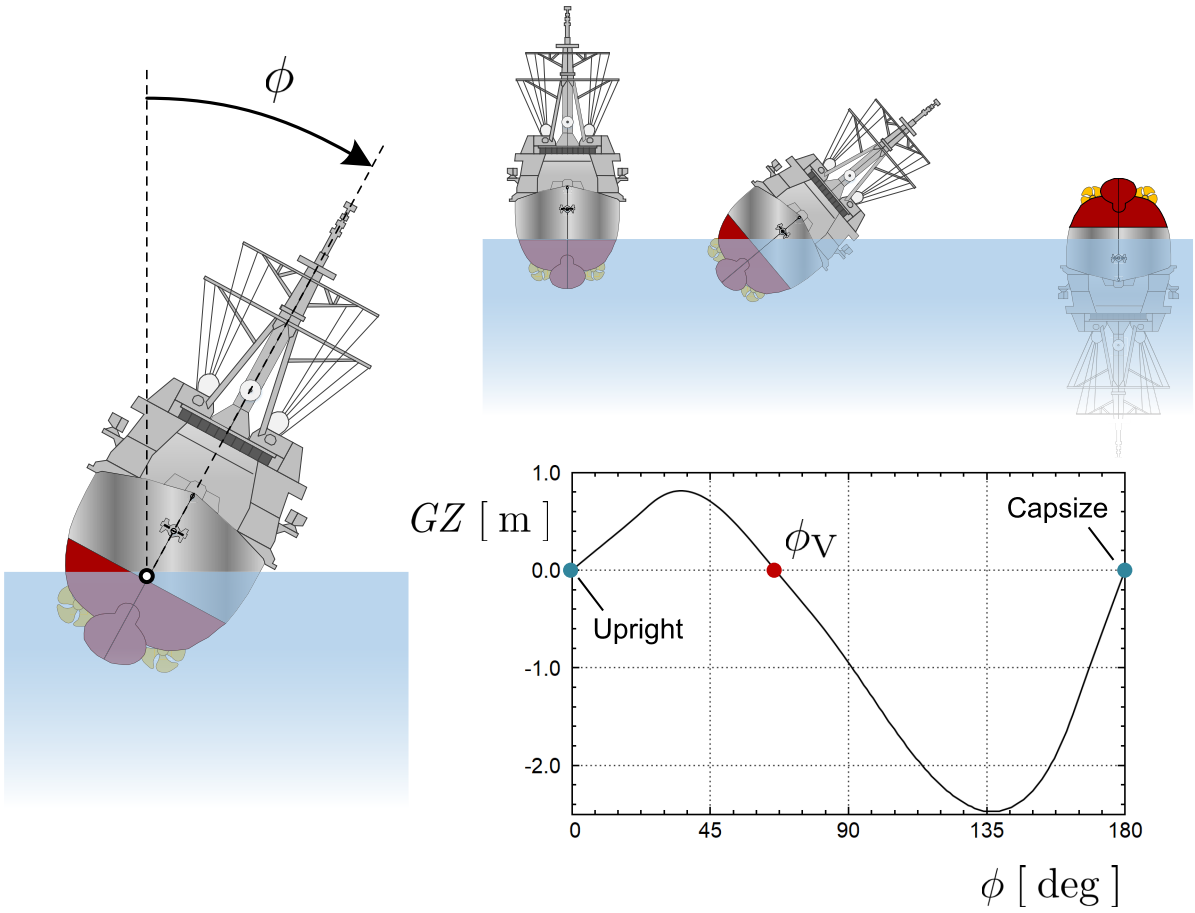

Fig. 3. Coordinate systems and example of GZ curve.

The severe wind and rolling criteria of the intact stability code were developed to guarantee the safety of ships against capsizing for ships losing all propulsive and steering power under wind and waves. In such a condition, the ship is known as a dead ship, and under no power to maintain its course, the ship could be in beam wind and wave condition [25]. In the weather criteria, the following equation of ship roll motion is used such as:

$$\ddot{\phi} + D(\dot{\phi}) + R(\phi) = K_{\text{wave}}(t) + K_{\text{wind}} \tag{3}$$

Here, $D(\dot{\phi})$, damping term; $R(\phi)$, restoring term; $K_{\text{wave}}(t)$, time-varying external moment term due to wave, K_{wind}, external moment term due to wind. Here the wave component is considered as sinusoidal function, and synchronous rolling motions are assumed. Since the motion is stationary, the energies concerning $D(\dot{\phi})$ and $K_{\text{wave}}(t)$ components could be cancelled out in one roll period. These are basic assumption of the criteria

The basic principle of this weather criteria is the energy balance of wind and restoring static moments under synchronous rolling motions. Figure 4 shows the key idea behind the weather criteria. In this figure, $\hat{\phi}$ indicates the shifted coordinate, D_{w} indicates the moment lever due to wind, and ϕ_{shifted} also indicates the heel angle (steady roll angle) due to wind moment lever D_{w}. Then, a ship is oscillated by incident waves around the drifted roll angle ϕ_{shifted} with the roll amplitude ϕ_{AW}. Now, c is defined as the ratio of the windward to the leeward areas of the restoring curve.

$$c \equiv \frac{\int_B^C GZ\left(\hat{\phi}\right)\mathrm{d}\hat{\phi}}{\int_B^D GZ\left(\hat{\phi}\right)\mathrm{d}\hat{\phi}} \tag{4}$$

Since $\int W \cdot GZ\,\mathrm{d}\phi$ is the potential energy, these areas denote the index of this energy. Under the

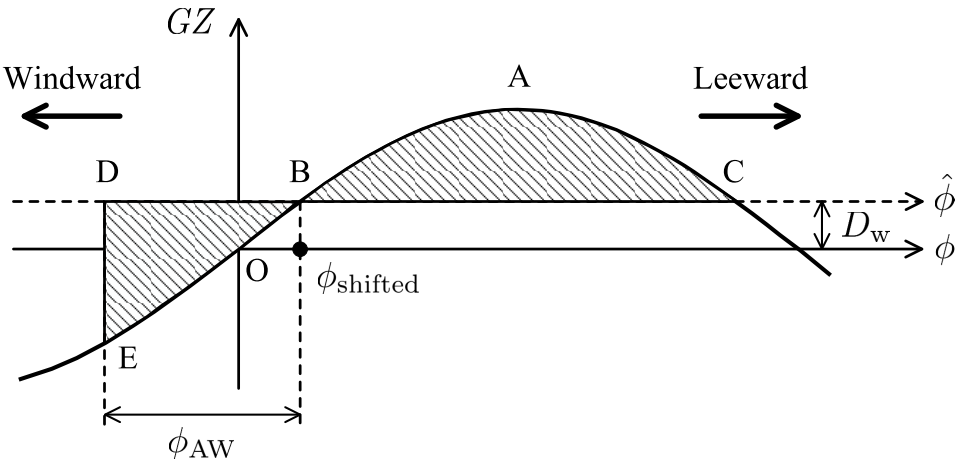

Fig. 4. Schematic of energy balance.

energy balance, the criteria require $c > 1$ or over for oceangoing vessels. The IMO weather criterion utilized is almost the same as the method adopted in Japan [26] without any major modification.

3. Complexity of motion in simple systems

The energy balance method explained above is well-constructed. By adopting this rule, there has been a remarkable record of no fatality due to the capsizing of Japanese-flagged passenger ships in Japan. However, with the development of the computer, in naval architecture, the mechanism of capsizing has been revealed to be more complicated than we had imagined. Figure 5 shows a good example of its complexity. It shows the initial condition that finally leads to capsizing for the following equation. In this figure, the white part means the capsizing. Here, κ is the roll-damping coefficient, and B is the amplitude of the external sinusoidal moment. This is a typical equation representing a motion of a vessel in a regular beam sea.

$$\ddot{\phi} + \kappa\dot{\phi} + \phi - \phi^3 = B\cos(\omega t + \delta) \tag{5}$$

As shown in Fig. 5, the shape of the capsizing boundary does not monotonically decrease, and fractal metamorphoses are not observed. Figure 6 is the magnified plot of Fig. 5. The inset of Fig. 6 is obtained by zooming in a small part. The plots show self-similarity. These facts indicate the complexity of the capsizing phenomenon in ships. Moreover, Fig. 7 indicates the capsizing boundary of control plane $(\omega, B)^T$. Each panel in this figure shows the result for different initial condition $(\phi(0), \dot{\phi}(0))^T$. Also in the control space, the capsizing boundary also shows the complexity. Therefore, capsizing cannot be predicted using the simple energy balance method.

As explained above, the *GZ* form of an actual vessel is complex to analyze. A simplified form of the *GZ* curve has been introduced for nonlinear analyses. Thompson employed the asymmetry-restoring curve having a quadratic form as follows [6, 7, 27]:

$$\ddot{x} + \beta\dot{x} + x - x^2 = F\sin(\Omega t) \tag{6}$$

Here, x is the main variable, β the damping coefficient, F the amplitude of the forcing term, and Ω the frequency of the forcing term. In this equation, the escape phenomenon, which is capsizing in a ship, happens. On the other hand, in naval engineering, the restoring term having cubic polynomial, as shown below, is used since ships *can* capsize to positive and negative sides.

Figure 8 shows the hull form of DTMB5415 in the left panel. In the right panel, the *GZ* curve obtained from the hydrostatic calculation is plotted as "Original" whereas the cubic polynomial approximation $c_1\phi - c_3\phi^3$ for the original *GZ* curve is done as "Fitted (cubic polynomial)." As can be seen here, cubic polynomial well approximated the original *GZ* curve.

The single degree of freedom (DoF) equation of motion in beam seas, which has cubic restoring curve, is expressed as follows:

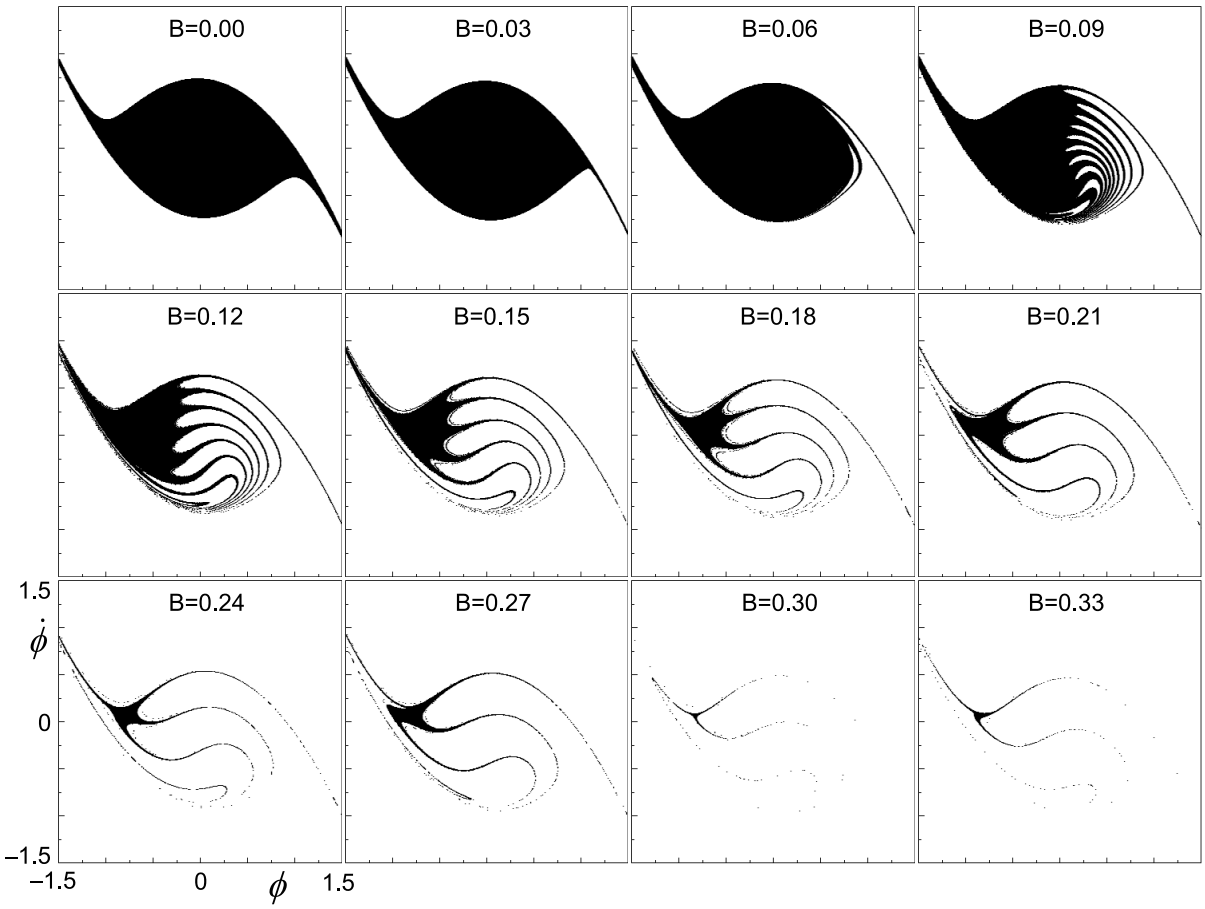

Fig. 5. Fractal metamorphoses of basin boundary in initial value plane with $\kappa = 0.04455$ and $\omega = 0.905$ (This figure duplicates Fig. 9 in the literature [14]), but at higher resolution).

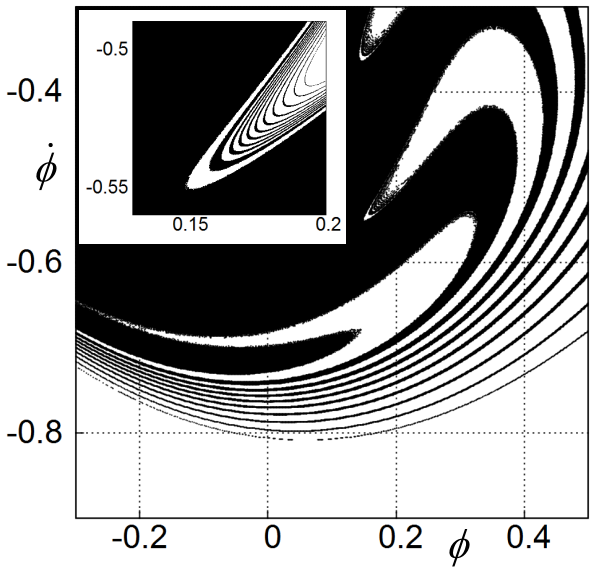

Fig. 6. Fractal magnification of metamorphoses of basin boundary in initial value plane with $\kappa = 0.04455$, $\omega = 0.905$ and $B = 0.09$ (This figure duplicates Fig. 10 in the literature [14]), but at higher resolution).

$$(I_{xx} + J_{xx})\,\ddot{\phi} + R \cdot \dot{\phi} + W \cdot GM \cdot \phi \left[1 - (\phi/\phi_V)^2\right] = M_0 + M\cos(\omega t + \delta) \tag{7}$$

where $\phi\,[\mathrm{rad}]$ denotes the instantaneous roll angle of the vessel and is a function of time $t\,[\mathrm{s}]$. $I_{xx}\,[\mathrm{kg}\cdot\mathrm{m}^2]$ and $J_{xx}\,[\mathrm{kg}\cdot\mathrm{m}^2]$ are the roll-directional and added moment of inertia, respectively,

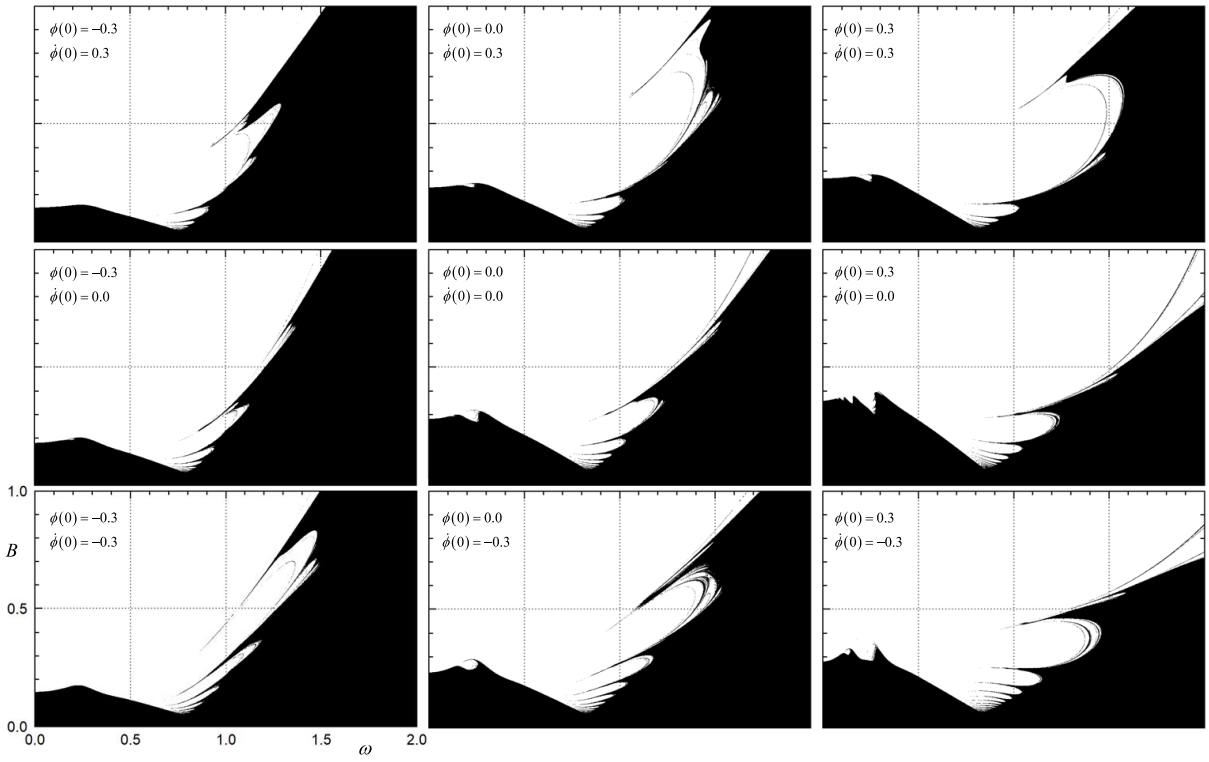

Fig. 7. Fractal metamorphoses of basin boundary in control space with $\kappa = 0.04455$ for different sets of initial values $\phi(0)$ and $\dot{\phi}(0)$ (The center figure ($\phi(0) = 0.0$ and $\dot{\phi}(0) = 0.0$) duplicates Fig. 12 in the literature [14], but at high resolution).

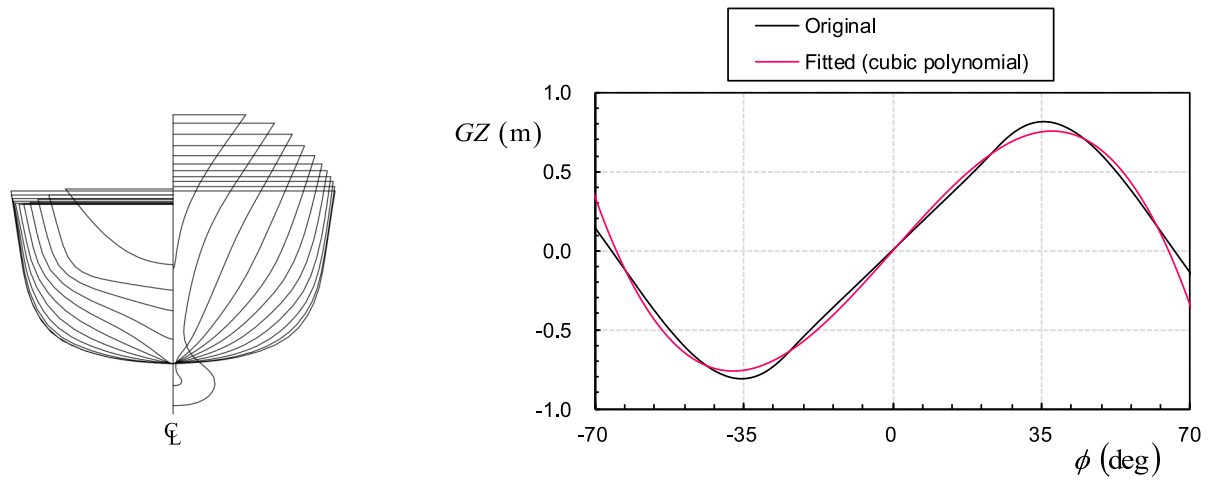

Fig. 8. Body plan of DTMB5415 hull form and its GZ curve. Here, cubic polynomial expression ($c_1\phi - c_3\phi^3$) is also plotted.

$R\,[\,\mathrm{kg}\cdot\mathrm{m}\cdot\mathrm{s}\,]$ is the roll-damping coefficient, and $GM\,[\,\mathrm{m}\,]$ is the metacentric height of the vessel. $\phi_V\,[\,\mathrm{rad}\,]$ is called the vanishing angle of the roll-restoring moment, and at $\pm\phi_V$, the restoring moment becomes zero. $M_0\,[\,\mathrm{kg}\cdot\mathrm{m}\,]$ and $M\,[\,\mathrm{kg}\cdot\mathrm{m}\,]$ denote constant wind-induced moment and amplitudes of time-varying wave-induced roll moments, respectively. $\omega\,[\,\mathrm{rad}\cdot\mathrm{s}^{-1}\,]$ is the wave frequency and δ is the phase of the wave-induced moment. Dividing both sides of (7) by the moment of inertia, $I_{xx} + J_{xx}$, the equation of motion becomes simple, as follows:

$$\ddot{\phi} + \kappa\dot{\phi} + c_1\phi - c_3\phi^3 = B_0 + B\cos(\omega t + \delta) \tag{8}$$

Where:

$$\begin{cases} \kappa \equiv \dfrac{R}{I_{xx}+J_{xx}}, c_1 \equiv \dfrac{W \cdot GM}{I_{xx}+J_{xx}}, c_3 \equiv \dfrac{W \cdot GM}{(I_{xx}+J_{xx})\,\phi_V^2} \\ B_0 \equiv \dfrac{M_0}{I_{xx}+J_{xx}}, B \equiv \dfrac{M}{I_{xx}+J_{xx}} \end{cases} \tag{9}$$

4. Analytical solution and its bifurcation

4.1 Analytical solution

First, we explain some analytical solutions for the case of $B_0 = 0$ and $\delta = 0$.

$$\ddot{\phi} + \kappa\dot{\phi} + c_1\phi - c_3\phi^3 = B\cos\omega t \tag{10}$$

This is a symmetric equation with respect to ϕ. In the harmonic balance method [2], the periodic solution $\phi_0(t)$ is assumed as:

$$\phi_0(t) = A\cos(\omega t + \epsilon) \tag{11}$$

Substituting this equation into Eq. (10) and comparing the coefficients of sinusoidal terms, the following equations are obtained [28]:

$$\begin{cases} \left[A\left(c_1 - \omega^2\right) - \dfrac{3}{4}A^3c_3\right]\sin\varepsilon + \kappa\omega A\cos\varepsilon = 0 \\ \left[A\left(c_1 - \omega^2\right) - \dfrac{3}{4}A^3c_3\right]\cos\varepsilon - \kappa\omega A\sin\varepsilon = B \end{cases} \tag{12}$$

$(c_1 - \omega^2)$ appeared in this equation is sometimes called "detuning parameter," please refer to [29]. From these equations, the relationship between the motion amplitude A and the amplitude of external moment B can be obtained as:

$$B^2 = A^2\left\{\left[\left(c_1 - \omega^2\right) - \frac{3}{4}A^2c_3\right]^2 + \kappa^2\omega^2\right\} \tag{13}$$

This is the well-known formula [28, 30], and the same results can be obtained using the averaging method by Krylov and Bogoliubov [31] and Hale [32].

4.2 Saddle-node bifurcation

The stability of the periodic solutions can be determined as shown in Hayashi [2]. Now, we introduce the nondimensional time $\tau = \omega t$. Then, the equation of motion becomes:

$$\ddot{\phi} + \beta\dot{\phi} + \alpha_1\phi + \alpha_3\phi^3 = B_1\cos\tau \tag{14}$$

where the coefficients are defined as

$$\beta = \frac{\kappa}{\omega}, \qquad \alpha_1 = \frac{c_1}{\omega^2}, \qquad \alpha_3 = -\frac{c_3}{\omega^2}, \qquad B_1 = \frac{B}{\omega^2}. \tag{15}$$

Here, the periodic solution of Eq. (14) is assumed to be $\phi_0(\tau)$. Since $\phi_0(\tau)$ is a solution of this system, it satisfies Eq. (14). Then, small perturbation from $\phi_0(\tau)$ is introduced as $\xi(\tau)$. Substituting $\phi(\tau) = \phi_0(\tau) + \xi(\tau)$ into Eq. (14), the equation for the perturbation system is obtained as:

$$\ddot{\xi} + \beta\dot{\xi} + \left(\alpha_1 + 3\alpha_3\phi_0^2\right)\xi = 0 \tag{16}$$

To eliminate the $\beta\dot{\xi}$ term, $\eta(\tau)$ is introduced.

$$\xi(\tau) = \exp\left(-\frac{1}{2}\beta\tau\right)\eta(\tau) \tag{17}$$

Then, the following system concerning $\eta(\tau)$ is obtained:

$$\ddot{\eta} + \left(\alpha_1 - \frac{1}{4}\beta^2 + 3\alpha_3\phi_0^2\right)\eta = 0 \tag{18}$$

Now, the periodic solution is defined as:

$$\phi_0(\tau) = A\cos(\tau - \varepsilon') \tag{19}$$

Substituting Eq. (19) to Eq. (18) yields:

$$\ddot{\eta} + (\theta_0 + 2\theta_1 \cos 2(\tau - \varepsilon'))\,\eta = 0 \tag{20}$$

$$\begin{cases} \theta_0 = \alpha_1 - \dfrac{1}{4}\beta^2 + \dfrac{3}{2}\alpha_3 A^2 \\ 2\theta_1 = \dfrac{3}{2}\alpha_3 A^2 \end{cases} \tag{21}$$

This is Mathieu's equation, and its stability diagram is shown in Fig. 9. If the following relation is satisfied, the periodic solution Eq. (20) becomes stable [2].

$$(\theta_0 - 1)^2 + 2(\theta_0 + 1)\beta^2 + \beta^4 > \theta_1^2 \tag{22}$$

In other words, the following condition is satisfied at the critical condition.

$$(\theta_0 - 1)^2 + 2(\theta_0 + 1)\beta^2 + \beta^4 = \theta_1^2 \tag{23}$$

This condition finally leads to

$$C^2 + \frac{3}{2}CA^2 + \kappa^2\omega^2 = 0 \tag{24}$$

$$C \equiv \omega^2 - 1 + \frac{3}{4}A^2 \tag{25}$$

On the other hand, when a saddle-node (fold) bifurcation occurs, the response curve satisfies the following "vertical tangent" condition (e.g. [11]):

$$\frac{\mathrm{d}B}{\mathrm{d}A} = 0 \tag{26}$$

From this condition, Eq. (24) is also derived.

Now, putting $R = A^2$, Eq. (13) can be expressed as

$$R^3 + a_2R^2 + a_1R + a_0 = 0 \tag{27}$$

where

$$a_2 = -\frac{24(c_1 - \omega^2)}{9c_3},\ a_1 = \frac{16\left[(c_1 - \omega^2)^2 + (\kappa\omega)^2\right]}{9c_3^2},\ a_0 = -\frac{16B^2}{9c_3^2}. \tag{28}$$

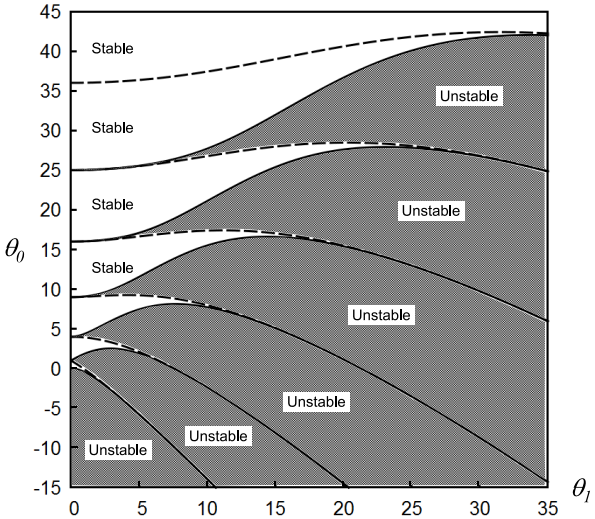

Fig. 9. Mathieu's stability diagram.

Introducing new variable $t = R + a_2/3$ yields

$$t^3 + a_1' t + a_0' = 0 \tag{29}$$

where

$$a_1' \equiv a_1 - \frac{a_2^2}{3},\ a_0' \equiv \frac{2a_2^3}{27} - \frac{a_2 a_1}{3} + a_0. \tag{30}$$

The discriminant D for Eq. (29) is:

$$D \equiv (t_1 - t_2)^2 (t_2 - t_3)^2 (t_3 - t_1)^2 \tag{31}$$

Here, t_1, t_2, t_3 are the solutions of Eq. (29). Considering

$$t_1 + t_2 + t_3 = 0, \quad t_1 t_2 + t_2 t_3 + t_3 t_1 = a_1', \quad t_1 t_2 t_3 = -a_0', \tag{32}$$

the discriminant D becomes

$$D = -\left(4{a_1'}^3 + 27{a_0'}^2\right) \tag{33}$$

Solving $D = 0$, the following condition is obtained as the fold bifurcation point for the designated B [14]:

$$B = \sqrt{\frac{8}{81 c_3}\left\{(c_1 - \omega^2)\left[(c_1 - \omega^2)^2 + 9\kappa^2\omega^2\right] \pm \left[(c_1 - \omega^2)^2 - 3\kappa^2\omega^2\right]^{3/2}\right\}} \tag{34}$$

Figure 10 shows the response amplitude curve. The folding of the response curves indicates the coexistence of multiple solutions. In the left panel, a numerical solution is shown, and they were obtained using Kawakami's method [33, 34]. In the right panel, the backbone curve is also plotted. The backbone curve can be obtained by putting $\kappa = 0$ and $B = 0$ into Eq. (13).

$$\omega^2 = c_1 - \frac{3}{4} c_3 A^2 \tag{35}$$

Due to this folding behavior of RAO, two different stable solutions are coexisting as shown in Fig. 11. The left panel of this figure shows the sets of initial conditions which converged to two different solutions. The right panel of this figure represents the numerically obtained boundary of initial condition sets. Here, the black points denote the saddle-type fixed points, and the solid lines do their stable manifolds. On the other hand, the white point also denotes the saddle point, and the dotted lines do its stable manifolds. As can be seen here, these stable manifolds become boundaries between capsizing and not-capsizing or between two different solutions. Although only in a few cases, the coexistence of multiple solutions has been experimentally observed [15]. Our research group has also measured this phenomenon. Figure 12 shows the response amplitude for different wave heights in

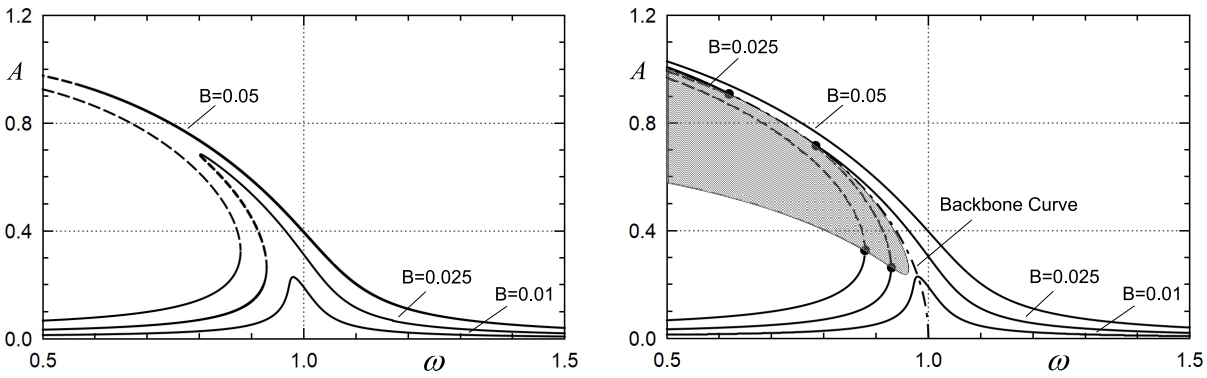

Fig. 10. Response amplitude of the primary motion with $c_1 = 1$, $c_3 = 1$, $\kappa = 0.04455$ and $B_0 = 0.0$. The left panel represents the numerical solutions, and the right panel shows the analytical solutions. The solid and dashed lines indicate the stable and unstable regions, respectively. (This figure duplicates Fig. 1 in the literature [24]).

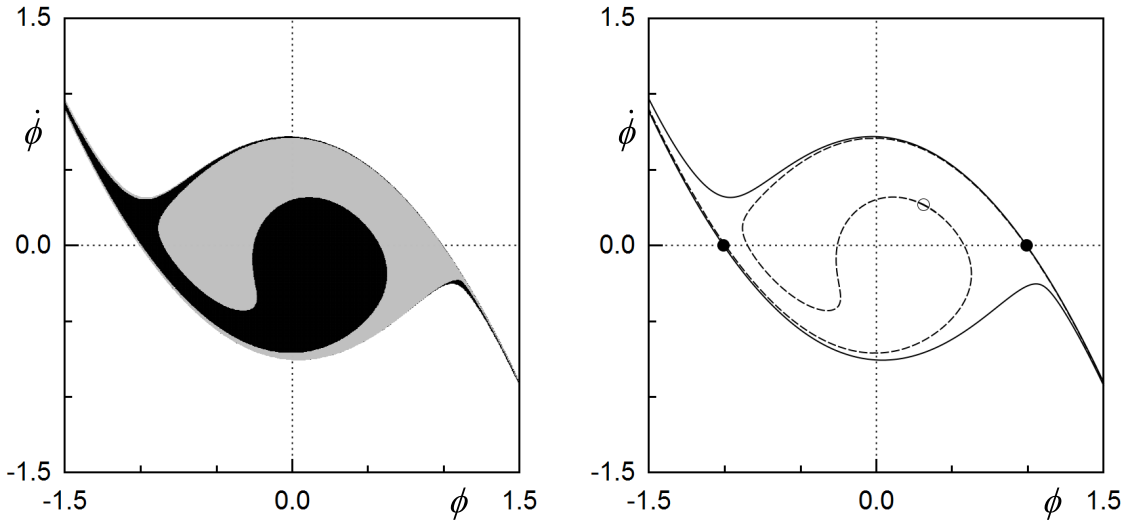

Fig. 11. Coexistence of the two solutions with $c_1 = 1$, $c_3 = 1$, $B = 0.025$, $\kappa = 0.04455$, $\omega = 0.905$. Black and gray regions show that with the initial conditions, the solution converges to a periodic attractor (fixed point, represented by the white points).

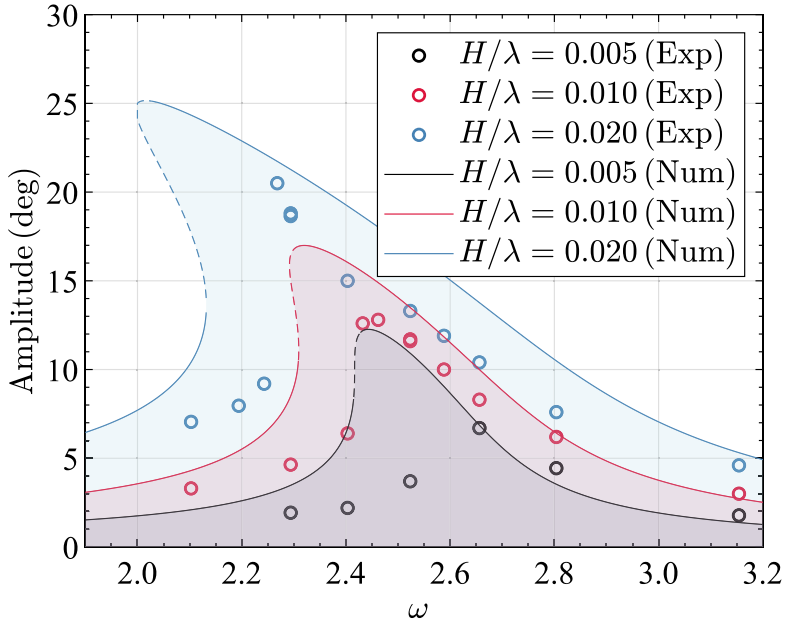

Fig. 12. Response amplitude of the model ship CEHIPAR2792. A part of the data is included in [36]. The lines show the results of the averaging method.

beam seas. This experiment was carried out at a rectangular tank of the National Research Institute of Fisheries Engineering (NRIFE). The subject ship was CEHIPAR2792 [35].

In the experiments, waves were generated by wavemakers in the model basin, and the frequency of the external force was not sequentially changed. After dissipating waves, waves for another condition were generated. Therefore, a sequential trace of the response curve was impossible. The photo of the experiment is shown in Fig. 13.

H and λ are the wave height and wavelength, respectively, and ω_0 is the natural roll frequency of the vessel. Under heavy wave conditions (higher H/λ condition), a jump in the response is observed. The theoretical results using the averaging method are also shown in the figure.

4.3 Negative stiffness in Mathieu's equation

Holmes and Rand [28] and Virgin [11] identified the bifurcation point from the condition of negative stiffness in Eq. (22). It corresponds to the 0th instability region in the Mathieu's equation, namely,

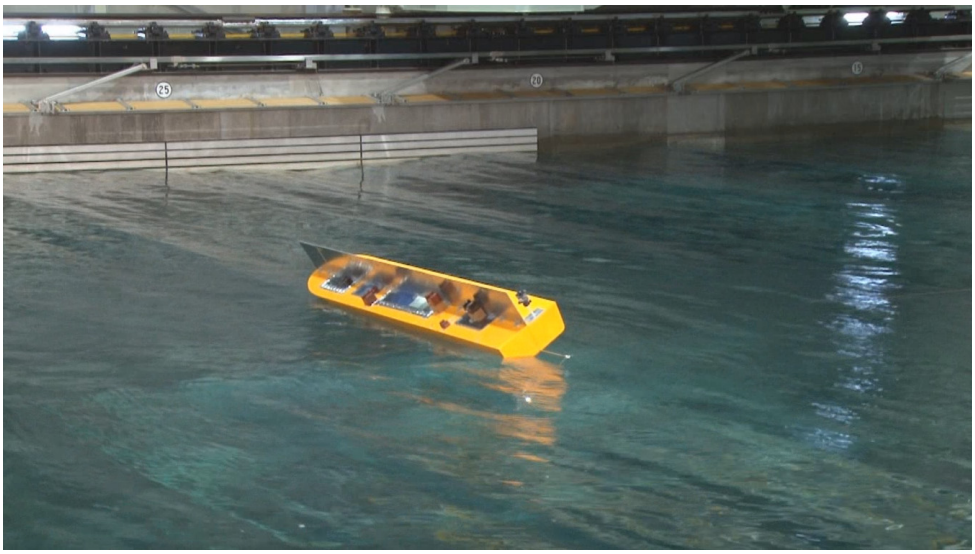

Fig. 13. Photo of the experiment for the model ship CEHIPAR2792 in the rectangular tank of the National Research Institute of Fisheries Engineering (NRIFE). Waves were generated by a wave maker located at the end of the tank (right side of this photo).

$\theta_0 < 0$. This condition becomes

$$\begin{aligned} \alpha_1 - \frac{1}{4}\beta^2 + \frac{3}{2}\alpha_3 A^2 < 0 \\ \Rightarrow A^2 > -\frac{2\alpha_1}{3\alpha_3}\left(1 - \frac{\beta^2}{4\alpha_1}\right) \end{aligned} \tag{36}$$

Note that α_3 is negative. Considering Eq. (15) yields:

$$A > \sqrt{\frac{2c_1}{3c_3}\left(1 - \frac{\kappa^2}{4c_1}\right)} \tag{37}$$

Usually, the damping term κ included in Eq. (37) is small in ship-roll motions; hence, κ^2 can be neglected. Thus, the threshold of the bifurcation approximately becomes

$$A = \sqrt{\frac{2c_1}{3c_3}} \tag{38}$$

Since c_3 is negative, this condition is never satisfied by the Duffing oscillator having a hard-type restoring moment. Substituting Eq. (38) into Eq. (13), we finally obtain the equation as follows:

$$B^2 = \frac{2c_1}{3c_3}\left[\left(\omega^2 - \frac{c_1}{2}\right)^2 + \kappa^2\omega^2\right] \tag{39}$$

4.4 Exceedance of vanishing stability angle

One of the fundamental criteria for capsizing is whether the motion amplitude is exceeded or not. Now, the stability vanishing angle is

$$\phi = \pm\sqrt{-\frac{\alpha_1}{\alpha_3}} \quad \text{or} \quad \phi = \pm\sqrt{\frac{c_1}{c_3}} \tag{40}$$

For this condition, the threshold of capsizing becomes

$$A = \sqrt{\frac{c_1}{c_3}} \tag{41}$$

This is the most "natural" condition for the safety of the ship.

4.5 Symmetry breaking and pitchfork bifurcation

The occasion of symmetry breaking was reported by some authors, including Kan [14]. Recently, the criterion for this phenomenon was shown in [24], and its symmetry breaking was finally concluded as the pitchfork bifurcation. The left panel in Fig. 14 shows the phase portrait of the coexistence of three solutions [24]. Two trajectories having larger amplitudes are asymmetric. The right panel in Fig. 14 shows an initial condition set for the three solutions. Red and blue regions indicate the two large-amplitude trajectories, and the gray region indicates the small-amplitude primary solution.

To show the condition of its occurrence, the same equation is employed, namely,

$$\ddot{\phi} + \kappa\dot{\phi} + c_1\phi - c_3\phi^3 = B\cos\omega t \tag{42}$$

The periodic solution with bias C_0 is assumed to be

$$\phi_b = C_0 + A\cos(\omega t + \varepsilon) \tag{43}$$

Substituting ϕ_b into Eq. (42), the following condition is obtained:

$$\begin{cases} C_0\left(c_1 - \dfrac{3}{2}c_3A^2 - C_0^2c_3\right) = 0 \\ A\left[(c_1-\omega^2) - \dfrac{3}{4}A^2c_3 - 3C_0^2c_3\right]\sin\varepsilon - \kappa\omega A\cos\varepsilon = 0 \\ A\left[(c_1-\omega^2) - \dfrac{3}{4}A^2c_3 - 3C_0^2c_3\right]\cos\varepsilon + \kappa\omega A\sin\varepsilon = B \end{cases} \tag{44}$$

If the amplitude satisfies

$$A = \sqrt{\frac{2c_1}{3c_3}} \tag{45}$$

in the first equation, the following equation is obtained:

$$C_0 = 0 \tag{46}$$

At this point, the pitchfork bifurcation occurs. The amplitude of the external wave moment after pitchfork bifurcation can be calculated as

$$B^2 = \frac{2c_1}{3c_3}\left[\left(\omega^2 - \frac{c_1}{2}\right)^2 + \kappa^2\omega^2\right] \tag{47}$$

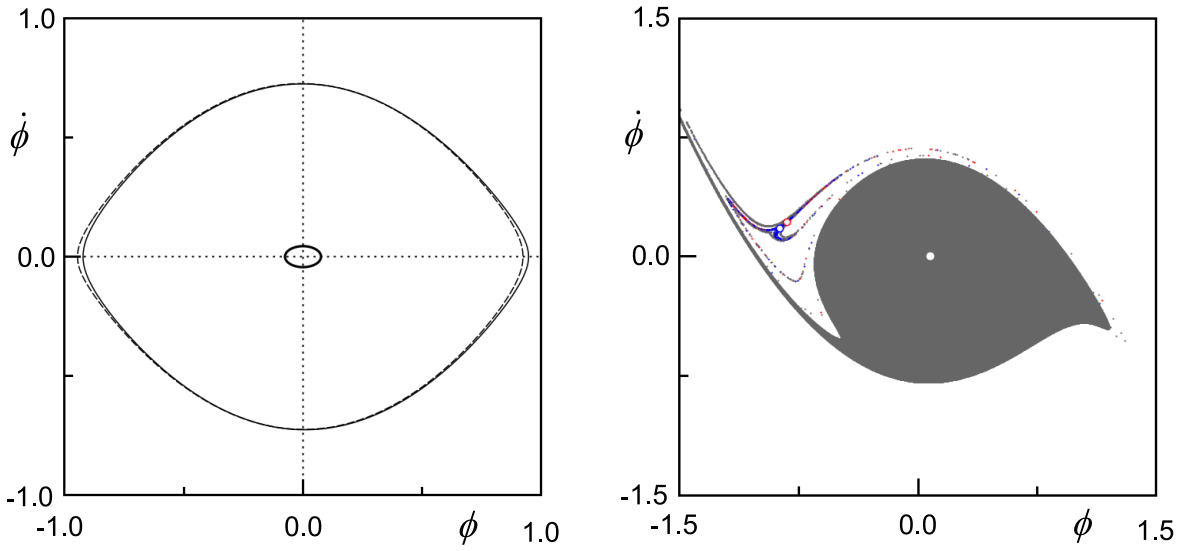

Fig. 14. Left panel: phase portraits of three trajectories [24]. Right panel: the convergence of an initial condition set for three solutions in a safe basin [24]. Both panels are the results with $c_1 = 1$, $c_3 = 1$, $\kappa = 0.04455$, $B = 0.05$, $B_0 = 0.0$, and $\omega = 0.579$.

This result is identical to Eq. (39). On the other hand, combining the second and third equations in Eq. (44), the amplitude of the motion is obtained as follows:

$$B^2 = A^2 \left\{ \left[\left(c_1 - \omega^2\right) - \frac{3}{4} c_3 \left(A^2 + 4C_0^2\right) \right]^2 + \kappa^2 \omega^2 \right\} \tag{48}$$

When C_0 takes a nonzero value, C_0 is obtained from the first equation in Eq. (44) as

$$C_0 = \pm \sqrt{\frac{c_1}{c_3} - \frac{3}{2} A^2} \tag{49}$$

This result indicates the existence of candidate two solutions for C_0: a positive or negative side shift with the same absolute value of the angle. Thus, the motions are identical to each other. Topologically, its symmetry in the positive and negative shifts can be explained by the symmetry of the dynamical system (Eq. (42)).

4.6 Global bifurcation

To theoretically estimate global bifurcation points, such as heteroclinic and homoclinic bifurcation, one of the best techniques is Melnikov's method [8, 9, 37]. The start of fractal metamorphoses in the safe-basin boundary is considered the global bifurcation. Therefore, as explained in the introduction part, Melnikov's method has been employed in several studies on capsizing, such as [7, 13, 16, 18].

To employ Melnikov's method, it is essential to calculate the separatrix connecting saddles for the Hamiltonian system, as follows:

$$\ddot{\phi} + c_1 \phi - c_3 \phi^3 = 0 \tag{50}$$

This autonomous system has two saddle points $\phi_s = \pm\sqrt{c_1/c_3}$. Here, we assume the form of the separatrix as $\dot{\phi} = C_s \left(\phi^2 - \phi_s^2\right)$. Substituting this assumed form into Eq. (50), we obtain the condition for C_s as $2C_s^2 = c_3$. Therefore, separatrix becomes:

$$\dot{\phi} = \pm \sqrt{\frac{c_3}{2}} \left(\phi^2 - \phi_s^2\right) \tag{51}$$

Equation (51) can be derived as follows. Multiplying $\dot{\phi}$ to both sides of Eq. (50) and integrating it in time yield:

$$\frac{1}{2}\dot{\phi}^2 + c_3 \left(\frac{1}{2}\phi^2 \phi_s^2 - \frac{1}{4}\phi^4 \right) = C_s' \tag{52}$$

C_s' can be determined by boundary condition $(\phi, \dot{\phi})^T = (\phi_s, 0)^T$. Then, the same form of separatrix Eq. (51) can be derived. Therefore, the separatrix for the system with $c_1 = 1$ and $c_3 = 1$ can be analytically obtained as:

$$\dot{\phi} = \pm \frac{1}{\sqrt{2}} \left(\phi^2 - 1\right) \quad \text{or} \quad \begin{cases} \phi = \tanh \dfrac{t}{\sqrt{2}} \\ \phi = \dfrac{1}{\sqrt{2}} \operatorname{sech}^2 \dfrac{t}{\sqrt{2}} \end{cases} \tag{53}$$

Figure 15 shows an example of the separatrix for the Hamiltonian system.

Hereafter, we explain the Melnikov integral. The state variable is defined as

$$\boldsymbol{x} = \begin{pmatrix} \phi \\ \dot{\phi} \end{pmatrix} \tag{54}$$

The differential equation is represented in the vector form as follows:

$$\dot{\boldsymbol{x}} = \boldsymbol{f}(\boldsymbol{x}) + \varepsilon \cdot \boldsymbol{g}(\boldsymbol{x}, t) \tag{55}$$

where $\boldsymbol{f}$ and $\boldsymbol{g}$ are expressed as

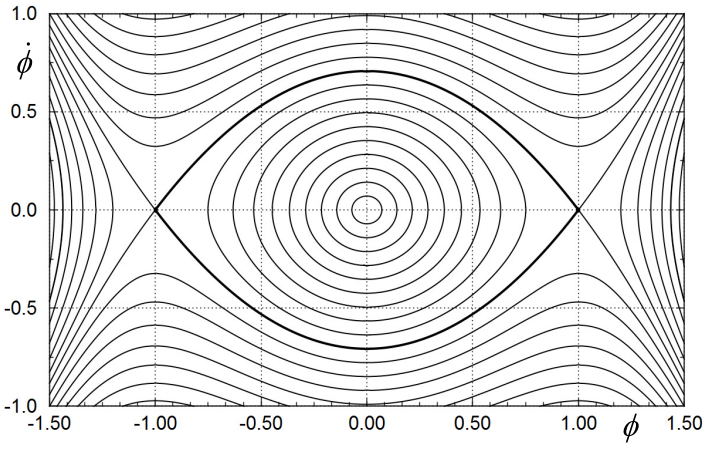

Fig. 15. Phase portrait for $\ddot{\phi} + \phi - \phi^3 = 0$.

$$\boldsymbol{f}(\boldsymbol{x}) = \begin{pmatrix} \dot{\phi} \\ -\phi + \phi^3 \end{pmatrix}, \quad \boldsymbol{g}(\boldsymbol{x}, t) = \begin{pmatrix} 0 \\ -\kappa\dot{\phi} + B\cos\omega t \end{pmatrix} \tag{56}$$

The Melnikov integral is defined as:

$$M(t_0) = -\int_{-\infty}^{\infty} \left[\boldsymbol{f}(\boldsymbol{x}_0(t)) \wedge \varepsilon \boldsymbol{g}(\boldsymbol{x}_0(t), t + t_0) \right] \mathrm{d}t \tag{57}$$

In this equation, $\boldsymbol{x}_0(t)$ is the separatrix for the Hamiltonian system. The separatrix $\boldsymbol{x}_0(t)$ is then

$$\boldsymbol{x}_0(t) = \begin{pmatrix} \tanh \dfrac{t}{\sqrt{2}} \\ \dfrac{1}{\sqrt{2}} \operatorname{sech}^2 \dfrac{t}{\sqrt{2}} \end{pmatrix} \tag{58}$$

The wedge product inside the integral is calculated as

$$\boldsymbol{f}(\boldsymbol{x}_0(t)) \wedge \varepsilon \boldsymbol{g}(\boldsymbol{x}_0(t), t + t_0) = \dot{\phi} \cdot \left(-\kappa\dot{\phi} + B\cos\omega(t + t_0) \right) \tag{59}$$

Thus, the Melnikov integral becomes

$$\begin{aligned} M(t_0) &= -\int_{-\infty}^{\infty} \left[\dot{\phi} \cdot \left(-\kappa\dot{\phi} + B\cos\omega(t + t_0) \right) \right] \mathrm{d}t \\ &= \sqrt{2} B \cos\omega t_0 \int_0^{\infty} \cos\omega t \cdot \operatorname{sech}^2 \left(\frac{t}{\sqrt{2}} \right) \mathrm{d}t - \kappa \int_0^{\infty} \operatorname{sech}^4 \left(\frac{t}{\sqrt{2}} \right) \mathrm{d}t \end{aligned} \tag{60}$$

The semi-infinite integral can be calculated in the complex domain as shown in Fig. 16.

$$\begin{cases} \displaystyle\int_0^{\infty} \cos\omega t \cdot \operatorname{sech}^2 \left(\frac{t}{\sqrt{2}} \right) \mathrm{d}t = \pi\omega \cdot \operatorname{cosech} \left(\frac{\pi\omega}{\sqrt{2}} \right) \\ \displaystyle\int_0^{\infty} \operatorname{sech}^4 \left(\frac{t}{\sqrt{2}} \right) \mathrm{d}t = \frac{2\sqrt{2}}{3} \end{cases} \tag{61}$$

Substituting Eq. (61) into Eq. (60), we obtain the final expression for B_M.

$$B_M = \frac{2\kappa}{3\pi\omega} \sinh \left(\frac{\pi\omega}{\sqrt{2}} \right) \tag{62}$$

As can be seen in Eq. (60), this integral can be regarded as an energy integral, and the condition $M(t_0) = 0$ means the energy balance of the dissipation term and external wave moment term on the separatrix. On the other hand, in the weather criteria, the same balance is imposed due to the assumption of the stational synchronous rollings. In the both, there could exist the similarity, and if so, the Melnikov's method to the ship safety criterion could be one of challenges.

We show an example with $\kappa = 0.04455$ and $\omega = 0.905$. In this case, the heteroclinic bifurcation point can be estimated as $B = 0.03830$. Figure 17 shows the change in the safe region, and it is

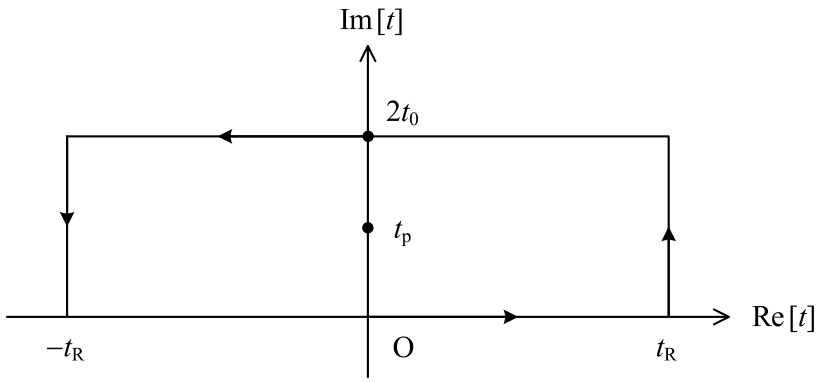

Fig. 16. Integral path of an infinite integral. $t_{\rm p}$ is a pole of integrand, and $t_{\rm R} \to \infty$ is finally taken.

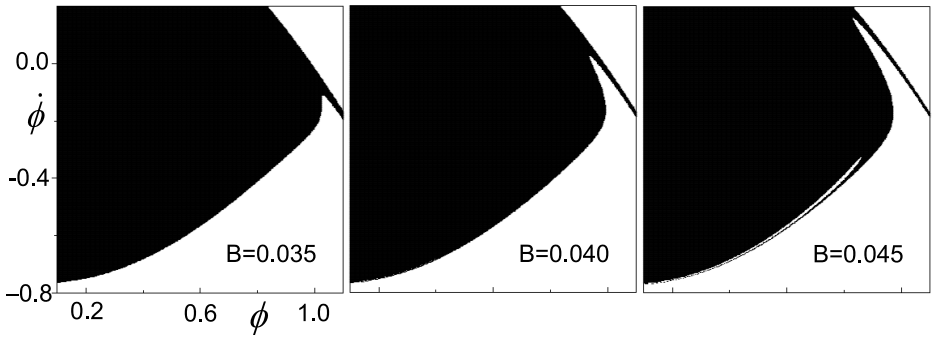

Fig. 17. Fractal metamorphoses of basin boundary in initial-value plane with $\kappa = 0.04455$. The threshold is calculated as $B = 0.03830$ from Eq. (62).

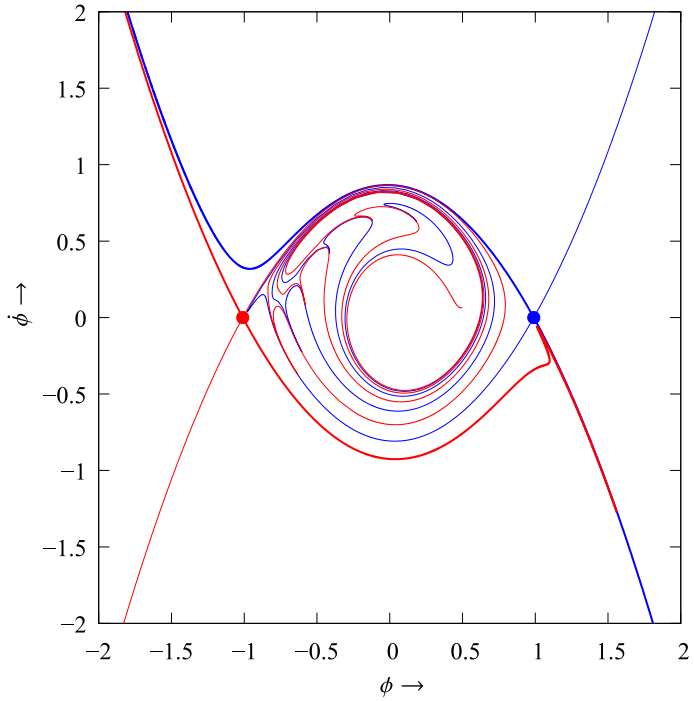

Fig. 18. Heteroclinic tangency with $\kappa = 0.04455$ and $B = 0.03830$ from Eq. (62). The blue and red curves are the manifolds for the blue and red saddles, respectively; thicker curves are the stable manifolds and thinner are the unstable ones.

observed that the erosion of the safe basin starts around B of 0.04. Figure 18 shows the Poincaré map at $B = 0.03830$, and it shows that this occurs immediately before the heteroclinic bifurcation. These show the validity of Melnikov's method.

In the case of high dissipation, the damping term cannot be regarded as a small order. For such a case, Melnikov's method for highly dissipative systems, proposed by Salam [38], is applicable. To apply this theory, the exact form of the heteroclinic or homoclinic orbits is necessary. Endo investigated the Melnikov integral for systems having piecewise linear restoring systems [39]. On the other hand, in general, a nonlinear differential equation is not solvable. To avoid such a challenge, Wu and McCue employed Melnikov's method for numerically obtained heteroclinic orbits [21]. On the other hand, owing to advances in nonlinear science, several solitary solutions have been found for nonlinear equations, such as literature [40]. Then, for a more general case, Maki et al. [22, 23] obtained the heteroclinic orbit for autonomous systems based on the solution method for nonlinear waves [41]. Suppose the following equation of motion with damping term.

$$\frac{\mathrm{d}^2\phi}{\mathrm{d}t^2} + \tilde{\beta}\frac{\mathrm{d}\phi}{\mathrm{d}t} + \tilde{\mu}\cdot\phi(1-\phi)(\phi-\hat{a}) = 0 \tag{63}$$

For the system (63), the following heteroclinic orbit is assumed:

$$\dot{\phi} = \tilde{c}\phi(1-\phi) \tag{64}$$

Solving Eq. (64), we obtain a time-domain solution as follows:

$$\phi^0(t) = \frac{1}{1+e^{-\bar{c}t+d}} = \frac{1}{2} + \frac{1}{2}\tanh\left(\frac{\bar{c}t-\tilde{d}}{2}\right) \tag{65}$$

Here, $\tilde{d} \in (-\infty, \infty)$ denotes the arbitrary integral constant determined by an initial condition, for instance, taking $\phi = 0.5$ at $t = 0$ yields $\tilde{d} = 0$. In this case, Eq. (64) becomes

$$\phi^0(t) = \frac{1}{2} + \frac{1}{2}\tanh\frac{\tilde{c}t}{2} \tag{66}$$

The proposed analytical method was validated with the numerical results of Wu and McCue [21], and the Melnikov integral was analytically determined with the use of Eq. (66).

5. Numerical analysis

In this section, we analyze the results of some numerical experiments to find the characteristic equation of ship motion (8).

5.1 Numerical example

Figure 19 compares the numerically obtained capsizing boundary and the analytically obtained bifurcation sets. The red line indicates the capsizing boundary for the initial condition, $\phi = 0.0$ and $\dot{\phi} = 0.0$. On the other hand, the "Numerical results of capsizing" are the numerically obtained capsizing threshold B. A periodic solution is traced with a slightly increasing the amplitude of the external force B until capsizing. Then, the obtained B is defined as the threshold.

Below $\omega = 1.0$, the saddle-node bifurcation lines coexist, indicating the coexistence of the periodic solutions. As stated by Kan and Taguchi [14], the saddle-node bifurcation line correspond to the red line (safe basin contour). Further, as also stated in [14], at a higher frequency region (above $\omega = 0.9$), the condition of capsizing (Eq. (41)), negative stiffness (Eq. (38)), and pitchfork (Eq. (45)) almost coincides with the tendency of the red line. The global bifurcation (heteroclinic bifurcation) set (Eq. (62)) always predicts the safe side.

5.2 Technical preliminaries

Using numerical integration, the Runge–Kutta method, we obtained the solution of Eq. (8) with an adequate step size. In addition, we define the Poincaré map T to discretize to treat the periodic orbits as a periodic map: $T : \mathbb{R}^2 \to \mathbb{R}^2; \boldsymbol{x}_0 \mapsto T(\boldsymbol{x}_0) = \boldsymbol{\varphi}(\boldsymbol{x}_0, 2\pi/\omega)$, where $\boldsymbol{x}_0$ is an initial value and $\boldsymbol{\varphi}(\boldsymbol{x}_0, t)$ is the trajectory function. The periodic orbit satisfying $\boldsymbol{\varphi}(\boldsymbol{x}_0, 2\pi\ell/\omega) = \boldsymbol{x}_0$ corresponds to the periodic point $\boldsymbol{x}_0$ satisfying $T^\ell(\boldsymbol{x}_0) = \boldsymbol{x}_0$.

The eigenvalues of $\partial T/\partial \boldsymbol{x}_0$ indicate the stability of the periodic point $\boldsymbol{x}_0$. In two-dimensional cases,

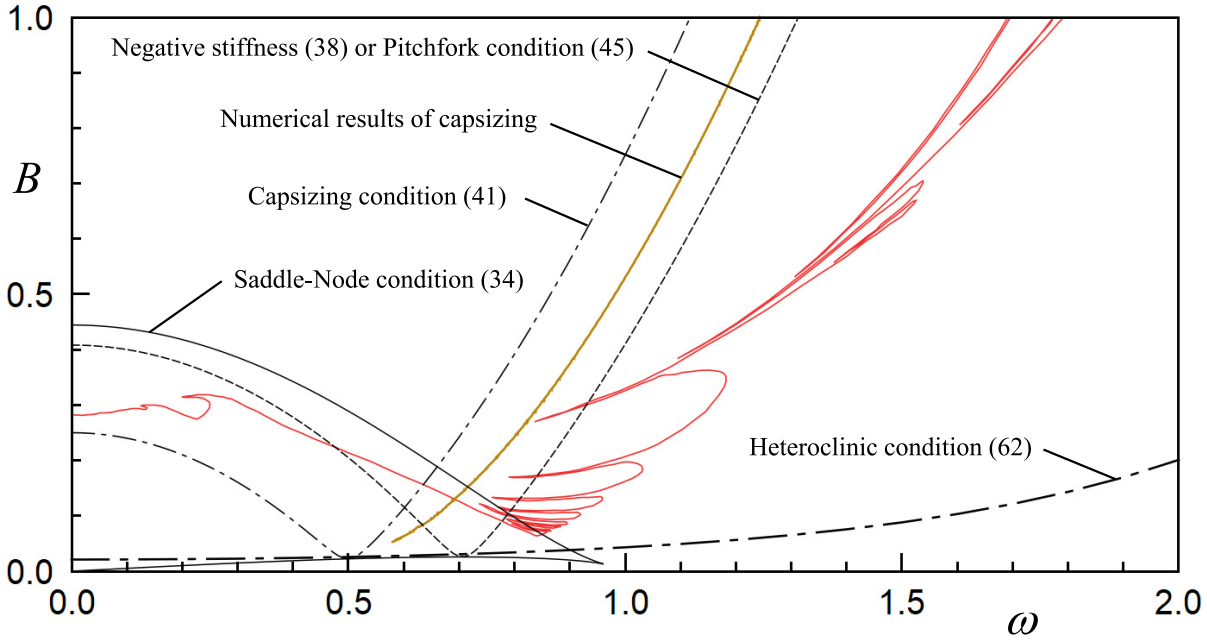

Fig. 19. Capsizing boundary and bifurcation sets with $c_1 = 1$, $c_3 = 1$. Red line indicates the capsizing boundary for $\phi = 0$ and $\dot{\phi} = 0$ shown in Fig. 7. The part of the plots is included in [24].

such as Eq. (8), two eigenvalues exist for one periodic point, including μ_1 and μ_2 with $\mu_1 < \mu_2$. The periodic point is a stable node, denoted as ${}_0D$, if $|\mu_1| < 1$ and $|\mu_2| < 1$; it is a saddle, denoted as ${}_1D$ or ${}_1I$, if $|\mu_1| > 1$ or $|\mu_2| > 1$; it is an unstable node, denoted ${}_2D$, if $|\mu_1| > 1$ and $|\mu_2| > 1$. According to the Liouville formula, system (8) does not contain the unstable node.

5.3 Stable and unstable manifolds

In the state space, stable and unstable manifolds of periodic points have great meaning. However, we need a special technique to calculate the manifolds of system (8) because the target periodic point often has several eigenvalues. Thus, we developed a method to calculate the stable and unstable manifolds in such a situation, as shown in Ref. [42]. The result obtained from the proposed method is as shown below.

Considering the case of the following parameters:

$$\kappa = 0.17,\ c_1 = 2,\ c_3 = 0.25,\ B_0 = 0,\ B = 0.6,\ \omega = 1.1.$$

Figure 20 shows the basin boundary in the initial-value plane calculated from the brute force method and the stable and unstable manifolds of two saddles calculated from the method of Ref. [42]. In the left-hand figure, the blue and red areas indicate the initial values where the trajectory converges to one and another periodic orbit, respectively. Choosing the initial values in the white region, the trajectory diverges. In the right-hand figure, the blue and red curves are the manifolds for the blue and red saddles, respectively. They complicatedly cross each other and form a fractal structure. We obtained these two results using completely different methods, but they show the same shape in the state space. This is because the stable manifolds of saddles generally form the basin boundary.

5.4 Bifurcation analysis

Stable and unstable manifolds change their form by controlling the system parameter. Processing the controlling, they can contact to each other and get crossed. This situation is the beginning of the erosion of the ship capsizing region and is known as one of the bifurcation phenomena. In the parameter plane, we confirm the bifurcation set where the qualitative change in the system occurs. In our previous study [43], some bifurcation sets of the system (8) were obtained with the parameters $\kappa = 0.05$, $c_1 = 1$, $c_3 = 1$, and $\omega = 1.0$, as shown in Fig. 21.

First, we confirm the symmetry of the system (8). This system is invariant under the following

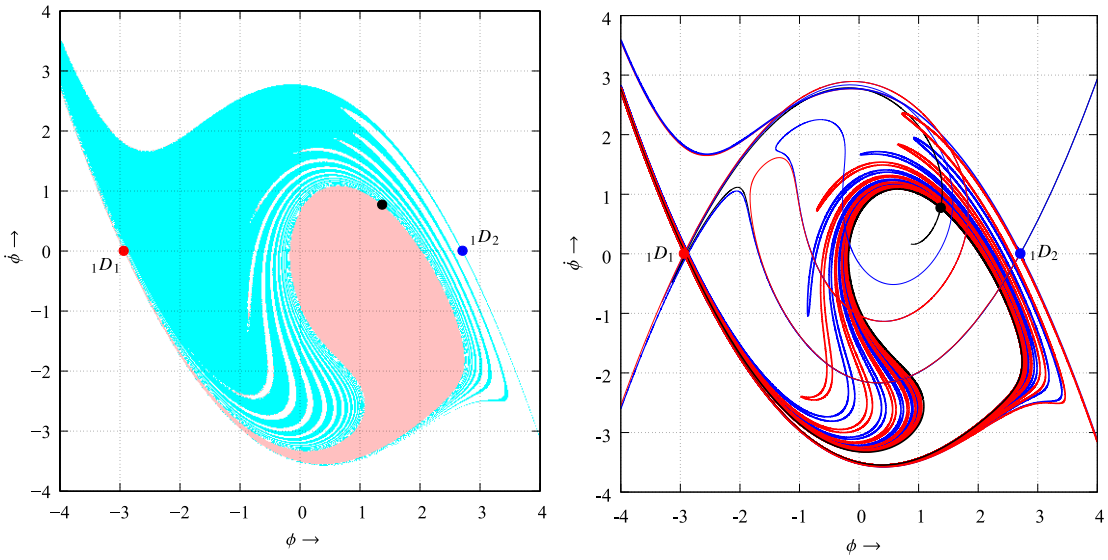

Fig. 20. Left panel: Fractal metamorphoses of basin boundary in the initial-value plane with $\kappa = 0.17$, $c_1 = 2$, $c_3 = 0.25$, $B_0 = 0$, $B = 0.6$, and $\omega = 1.1$ (This figure duplicates Fig. 12 in the literature [10]), but at a higher resolution). Right panel: stable and unstable manifolds of two saddles, $_1D_1$ and $_1D_2$, which are the red and blue points, respectively. Bolder curves are the stable manifolds and thinner curves are the unstable manifolds.

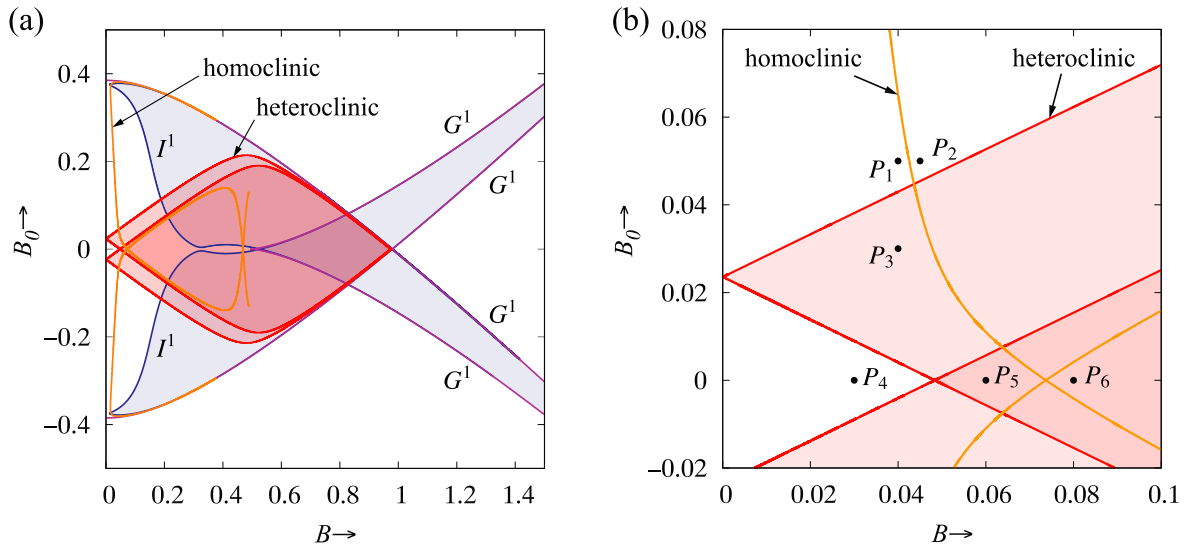

Fig. 21. Bifurcation sets of the system (8) with $\kappa = 0.5$, $c_1 = 1$, $c_3 = 1$ and $\omega = 1.0$ (this figure duplicates Fig. 1 in the literature [43]). G^1 and I^1 are saddle-node and period-doubling bifurcation sets, respectively.

transformation:

$$\begin{bmatrix} \phi \\ t \\ B_0 \end{bmatrix} \mapsto \begin{bmatrix} -\phi \\ t + \pi/\omega \\ -B_0 \end{bmatrix}.$$

Therefore, when we find a periodic orbit with some B_0, we can also observe another periodic orbit having the same topological structure as $-B_0$. In other words, the two symmetric orbits have completely the same stability so that the bifurcation diagram is symmetric to $B_0 = 0$, as shown in Fig. 21(a). In the case of $B_0 = 0$, the two periodic orbits coexist in the same state space and encounter the bifurcation set simultaneously. This leads to the lined-up cross points of the bifurcation curves on the line $B_0 = 0$.

Next, let us discuss Fig. 21. As a parameter changes, the periodic orbit continuously changes its

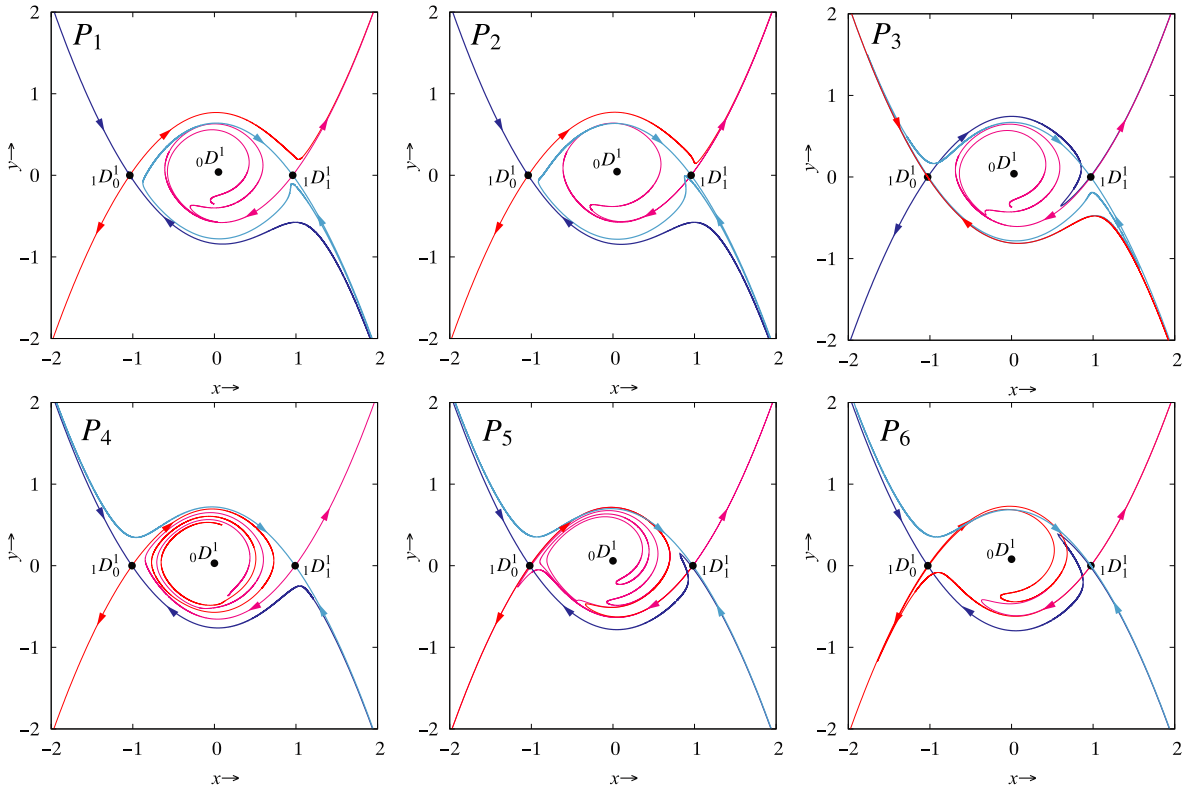

Fig. 22. Stable and unstable manifolds of the system (8) with the parameters of P_1–P_6. This figure duplicates Fig. 5 in the literature [43] and the variables x and y here are equivalent to the variables ϕ and $\dot{\phi}$ in this manuscript, respectively.

position and suddenly disappear at a critical value of the parameter. The set of parameters is the local bifurcation set, shown as G^1 or I^1. In the reverse process, the periodic orbit suddenly appears. As a parameter changes again, stable and unstable manifolds cross each other. The parameter set where the two manifolds cross each other is the global bifurcation set, denoted as homoclinic and heteroclinic. The global bifurcation relates to the structure of the stable manifold and, therefore, causes a crucial change in the basin boundary. Figure 22 shows the structure of the stable manifolds for each point in Fig. 21(b). On the heteroclinic bifurcation between P_4 and P_5, erosion of the divergent region into the convergent region progresses when global bifurcation occurs.

6. Further topics on ship capsizing

The actual seaway in the ocean is not a regular phenomenon. Studies combining the theories of nonlinear dynamics and stochastics have been conducted in the naval architecture field. In this section, we briefly introduce their contributions.

So far, a considerable number of theoretical studies on ship motions in irregular seas have been conducted. Haddara employed the Fokker-Planck-Kolmogorov (FPK) equation to estimate the value and variance of ship-roll motion in beam seas [44]. Roberts combined the averaging method and FPK equation to derive the probability density function (PDF) of roll motion in beam seas [45]. The results were compared with the numerical PDF of roll motion reported by Dalzell [46]. Fujiwara et al. [47] conducted a model experiment on capsizing in the towing tank of Osaka Prefecture University, and the results were compared with the theoretical results reported by Umeda [48]. Belenky applied piecewise linearization to the *GZ* curve and obtained the theoretical method for predicting the probability of capsizing. In the 21st century, research on the probability of capsizing and ship motion has been further advanced. Dostal et al. presented an energy-based averaging method, and the prediction accuracy of the PDF of roll motion was enhanced [49, 50]. The authors [36, 51] also developed a method for predicting the PDF of roll motion based on Kimura's work [52, 53], and the probability

of capsizing was successfully predicted for general 1 DoF roll equation of motion [51]. However, the theoretical approach to predicting the probability of capsizing for the multi-DoF equation of motion is challenging, and it shall be considered in our future studies.

7. Conclusion

In this paper, we discuss the dynamics of the capsizing of a vessel in seas. One of the characteristics of the equations of ship motion is the soft-spring stiffness in its restoring moment. Owing to these characteristics, the analysis for capsizing is not straightforward, and complex phenomena occur. We discuss some criteria for the theoretical estimation of the capsizing boundaries, and numerical results are presented. Further, the mechanism of global bifurcation is explained in detail. The period-doubling bifurcation that happens immediately after pitchfork bifurcation is not discussed here; it shall be analyzed in our future studies.

For practical application of the results, there is a need to extend the theories to multidimensional equations of motion and irregular external moments. We aim at the application of these results in future ship safety criteria and designs.

From the point of view of nonlinear dynamics, the capsizing of oceangoing vessels has been studied in naval architecture and ocean engineering since the mid-1980s. This topic has a very long history, and we believe it still strongly attracts several researchers.

Acknowledgments

This work was supported by a Grant-in-Aid for Scientific Research from the Japan Society for Promotion of Science (JSPS KAKENHI Grant Numbers JP19H02360, JP21K14362). The authors are grateful to Mr. Colin Langilangi and Mr. Sreenath Subramaniam of Osaka University for making Fig. 7. The authors are also thankful to Enago (www.enago.jp) for reviewing the English language.

References

[1] S. Consortium *et al.*, "Final report–research study on the sinking sequence of mv estonia," tech. rep., SSPA Research Report, 2008.

[2] C. Hayashi, Nonlinear oscillations in physical systems, Princeton University Press, 2014.

[3] A. Nayfeh and A. Khdeir, "Nonlinear rolling of ships in regular beam seas," *International Shipbuilding Progress*, vol. 33, no. 379, pp. 40–49, 1986.

[4] A. Nayfeh and A. Khdeir, "Nonlinear rolling of biased ships in regular beam waves," *International Shipbuilding Progress*, vol. 33, no. 381, pp. 84–93, 1986.

[5] A. Nayfeh and N. Sanchez, "Chaos and dynamic instability in the rolling motion of ships," *Symposium on Naval Hydrodynamics*, 17th, 1988.

[6] J. Thompson, S. Bishop, and L. Leung, "Fractal basins and chaotic bifurcations prior to escape from a potential well," *Physics Letters A*, vol. 121, no. 3, pp. 116–120, 1987.

[7] J.M.T. Thompson, "Chaotic phenomena triggering the escape from a potential well," *Proceedings of the Royal Society of London. A. Mathematical and Physical Sciences*, vol. 421, no. 1861, pp. 195–225, 1989.

[8] J. Guckenheimer and P. Holmes, *Nonlinear oscillations, dynamical systems, and bifurcations of vector fields*, vol. 42, Springer Science & Business Media, 2013.

[9] B. Greenspan and P. Holmes, "Repeated resonance and homoclinic bifurcation in a periodically forced family of oscillators," *SIAM Journal on Mathematical Analysis*, vol. 15, no. 1, pp. 69–97, 1984.

[10] L. Virgin, "The nonlinear rolling response of a vessel including chaotic motions leading to capsize in regular seas," *Applied Ocean Research*, vol. 9, no. 2, pp. 89–95, 1987.

[11] L. Virgin, "On the harmonic response of an oscillator with unsymmetric restoring force," *Journal of Sound and Vibration*, vol. 126, no. 1, pp. 157–165, 1988.

[12] L. Virgin and S. Bishop, "Complex dynamics and chaotic responses in the time domain simulations of a floating structure," *Ocean Engineering*, vol. 15, no. 1, pp. 71–90, 1988.

[13] M. Kan, T. Saruta, H. Taguchi, and M. Yasuno, "Capsizing of a ship in quatering seas part 1.

Model experiments on mechanism of capsizing," *Journal of the Society of Naval Architects of Japan*, vol. 1990, no. 167, pp. 81–90, 1990.
[14] M. Kan and H. Taguchi, "Capsizing of a ship in quatering seas part 2. Chaos and fractal in capsizing phenomenon," *Journal of the Society of Naval Architects of Japan*, vol. 1990, no. 168, pp. 211–220, 1990.
[15] A. Francescutto, G. Contento, and R. Penna, "Experimental evidence of strongly nonlinear effects in the rolling motion of a destroyer in beam sea," *STAB '94*, pp. 1–25, Florida Institute of Technology, 1994.
[16] J.M. Falzarano, S.W. Shaw, and A.W. Troesch, "Application of global methods for analyzing dynamical systems to ship rolling motion and capsizing," *International Journal of Bifurcation and Chaos*, vol. 2, no. 01, pp. 101–115, 1992.
[17] M. Bikdash, B. Balachandran, and A. Navfeh, "Melnikov analysis for a ship with a general roll-damping model," *Nonlinear Dynamics*, vol. 6, no. 1, pp. 101–124, 1994.
[18] S.R. Hsieh, A.W. Troesch, and S.W. Shaw, "A nonlinear probabilistic method for predicting vessel capsizing in random beam seas," *Proceedings of the Royal Society of London. Series A: Mathematical and Physical Sciences*, vol. 446, no. 1926, pp. 195–211, 1994.
[19] S. Murashige and K. Aihara, "Experimental study on chaotic motion of a flooded ship in waves," *Proceedings of the Royal Society of London. Series A: Mathematical, Physical and Engineering Sciences*, vol. 454, no. 1978, pp. 2537–2553, 1998.
[20] S. Murashige, T. Yamada, and K. Aihara, "Nonlinear analyses of roll motion of a flooded ship in waves," *Philosophical Transactions of the Royal Society of London. Series A: Mathematical, Physical and Engineering Sciences*, vol. 358, no. 1771, pp. 1793–1812, 2000.
[21] W. Wu and L. McCue, "Application of the extended Melnikov's method for single-degree-of-freedom vessel roll motion," *Ocean Engineering*, vol. 35, no. 17-18, pp. 1739–1746, 2008.
[22] A. Maki, N. Umeda, and T. Ueta, "Melnikov integral formula for beam sea roll motion utilizing a non-Hamiltonian exact heteroclinic orbit," *Journal of Marine Science and Technology*, vol. 15, no. 1, pp. 102–106, 2010.
[23] A. Maki, N. Umeda, and T. Ueta, "Melnikov integral formula for beam sea roll motion utilizing a non-Hamiltonian exact heteroclinic orbit: Analytic extension and numerical validation," *Journal of Marine Science and Technology*, vol. 19, no. 3, pp. 257–264, 2014.
[24] A. Maki, L. Virgin, N. Umeda, T. Ueta, Y. Miino, M. Sakai, and H. Kawakami, "On the loss of stability of periodic oscillations and its relevance to ship capsize," *Journal of Marine Science and Technology*, vol. 24, no. 3, pp. 846–854, 2019.
[25] IMO, *International code on intact stability*, 2008, Inter-Governmental Maritime, 2009.
[26] M. Sato, Y. Yamanouchi, S. Motora, and M. Uchida, "A proposed standard of stability for passenger ships part II: Small crafts," *Journal of Zosen Kiokai*, vol. 1955, no. 96, pp. 25–30, 1955.
[27] J. Thompson and Y. Ueda, "Basin boundary metamorphoses in the canonical escape equation," *Dynamics and Stability of Systems*, vol. 4, no. 3-4, pp. 285–294, 1989.
[28] P. Holmes and D. Rand, "The bifurcations of Duffing's equation: An application of catastrophe theory," *Journal of Sound and Vibration*, vol. 44, no. 2, pp. 237–253, 1976.
[29] J.A. Sanders, F. Verhulst, and J. Murdock, *Averaging methods in nonlinear dynamical systems*, vol. 59, Springer, 2007.
[30] L.N. Virgin, "Approximate criterion for capsize based on deterministic dynamics," *Dynamics and Stability of Systems*, vol. 4, no. 1, pp. 56–70, 1989.
[31] N.M. Krylov and N.N. Bogoliubov, *Introduction to non-linear mechanics*, no. 11, Princeton University Press, 1950.
[32] J.K. Hale, *Ordinary Differential Equations*, Wiley-Interscience, New York, 1969.
[33] H. Kawakami, "Bifurcation of periodic responses in forced dynamic nonlinear circuits: Computation of bifurcation values of the system parameters," *IEEE Transactions on Circuits and Systems*, vol. 31, no. 3, pp. 248–260, 1984.
[34] K. Tsumoto, T. Ueta, T. Yoshinaga, and H. Kawakami, "Bifurcation analyses of nonlinear

dynamical systems: From theory to numerical computations," *NOLTA*, vol. 3, no. 4, pp. 458–476, 2012.

[35] G. Bulian, A. Francescutto, and F. Fucile, "An experimental investigation in the framework of the alternative assessment for the IMO weather criterion," *Proc. of the HYDRALAB III Joint User Meeting*, 2010.

[36] A. Maki, N. Umeda, A. Matsuda, and H. Yoshizumi, "Non-Gaussian PDF of ship roll motion in irregular beam sea and wind conditions-comparison between theory and experiment," *Ocean Engineering*, vol. 188, 106278, 2019.

[37] P.J. Holmes, "Averaging and chaotic motions in forced oscillations," *SIAM Journal on Applied Mathematics*, vol. 38, no. 1, pp. 65–80, 1980.

[38] F.M. Salam, "The Mel'nikov technique for highly dissipative systems," *SIAM Journal on Applied Mathematics*, vol. 47, no. 2, pp. 232–243, 1987.

[39] T. Endo, L.O. Chua, and T. Narita, "Chaos from phase-locked loops. High-dissipation case," *IEEE Transactions on Circuits and Systems*, vol. 36, no. 2, pp. 255–263, 1989.

[40] N.A. Kudryashov, "Exact solitary waves of the Fisher equation," *Physics Letters A*, vol. 342, no. 1-2, pp. 99–106, 2005.

[41] X. Wang, Z. Zhu, and Y. Lu, "Solitary wave solutions of the generalised Burgers-Huxley equation," *Journal of Physics A: Mathematical and General*, vol. 23, no. 3, pp.271–274, 1990.

[42] Y. Miino, T. Ueta, A. Maki, N. Umeda, and H. Kawakami, "A computation method to calculate the stable manifold of a ship dynamical system," *Proceedings of 2019 IEICE NOLTA Society Conference*, vol.NLS, Nagaoka, Japan, p.12, 6 2019.

[43] Y. Miino, T. Ueta, H. Kawakami, A. Maki, and N. Umeda, "Local stability and bifurcation analysis of the softening Duffing equation by numerical computation," *Proceedings of International Conference on the Stability of Ships and Ocean Vehicles*, Kobe, Japan, pp. 16–21, 9 2018.

[44] M.R. Haddara, "A modified approach for the application of Fokker-Plank equation to the nonlinear ship motions in random waves," *International Shipbuilding Progress*, vol. 21, no. 242, pp. 283–288, 1974.

[45] J. Roberts *et al.*, "A stochastic theory for nonlinear ship rolling in irregular seas," *Journal of Ship Research*, vol. 26, no. 04, pp. 229–245, 1982.

[46] J. Dalzell, "A note on the distribution of maxima of ship rolling," *Journal of Ship Research*, vol. 17, no. 04, pp. 217–226, 1973.

[47] T. Fujiwara, Y. Ikeda, and N. Umeda, "Stability assessment of a ship by applying risk analysis based on the capsizing probability," *Journal of the Kansai Society of Naval Architects, Japan*, vol. 221, no. 0, pp. 111–116, 1994.

[48] N. Umeda, Y. Ikeda, and S. Suzuki, "Risk analysis applied to the capsizing of high-speed craft in beam seas," *Proceedings of the 5th International Symposium on the Practical Design of Ships and Mobile Units*, vol. 2, pp. 1131–1145, 1992.

[49] L. Dostal, E. Kreuzer, and N. Sri Namachchivaya, "Non-standard stochastic averaging of large-amplitude ship rolling in random seas," *Proceedings of the Royal Society A: Mathematical, Physical and Engineering Sciences*, vol. 468, no. 2148, pp. 4146–4173, 2012.

[50] L. Dostal and E. Kreuzer, "Assessment of extreme rolling of ships in random seas," *ASME 2014 33rd International Conference on Ocean, Offshore and Arctic Engineering*, American Society of Mechanical Engineers Digital Collection, 2014.

[51] A. Maki, "Estimation method of the capsizing probability in irregular beam seas using non-Gaussian probability density function," *Journal of Marine Science and Technology*, vol. 22, no. 2, pp. 351–360, 2017.

[52] K. Kimura, M. Komada, and M. Sakata, "Non-Gaussian equivalent linearization for estimation of stochastic response distribution of nonlinear systems," *Transactions of the Japan Society of Mechanical Engineers, Series C*, vol. 61, no. 450, pp. 278–287, 1995.

[53] K. Kimura and T. Morimoto, "Estimation of non-Gaussian response distribution of a nonlinear system subjected to random excitation (application to nonwhite excitation with nonrational spectrum)," *J. Jpn. Soc. Mech. Eng.*, vol. 64, no. 617, pp. 1–6, 1998.